REPORT DOCUMENTATION PAGE Dist: A

Form Approved
OMB No. 0704-0188

1. AGENCY USE ONLY (Leave blank)	2. REPORT DATE	3. REPORT TYPE AND DATES COVERED
	Dec 94	Final 01 NOV 93 - 31 OCT 94

4. TITLE AND SUBTITLE
Direct Numerical Simulation of Compressible Turbulent Flows Using adaptive Spectral Element Method

5. FUNDING NUMBERS
F49620-93-1-0020
2307/AS

6. AUTHOR(S)
T. J. Chung and K. T. Yoon

7. PERFORMING ORGANIZATION NAME(S) AND ADDRESS(ES)
U Alabama @ Huntsville
Dept of Mech Eng
Huntsville AL 35899

8. PERFORMING ORGANIZATION REPORT NUMBER
AFOSR-TR- 95 0051

9. SPONSORING/MONITORING AGENCY NAME(S) AND ADDRESS(ES)
AIR FORCE OFFICE OF SCIENTIFIC RESEARCH
DIRECTORATE OF AEROSPACE SCIENCES
BOLLING AFB, DC 20332-6448

10. SPONSORING/MONITORING AGENCY REPORT NUMBER
F49620-93-1-0020
2307/AS

11. SUPPLEMENTARY NOTES

12a. DISTRIBUTION/AVAILABILITY STATEMENT
APPROVED FOR PUBLIC RELEASE
DISTRIBUTION IS UNLIMITED

12b. DISTRIBUTION CODE
A

13. ABSTRACT (Maximum 200 words)

In this final report covering the period 1993-1994, the preliminary results of the research on direct numerical simulation of compressible turbulent flows are presented. Specifically, the adaptive Legendre polynomial spectral element method with the mixed explicit-implicit(MEI) Taylor-Galerkin formulation is used in order to capture detailed physics involved in three-dimensional shock wave turbulent boundary layer interactions.

14. SUBJECT TERMS	15. NUMBER OF PAGES
Spectral Element, DNS	38
	16. PRICE CODE

17. SECURITY CLASSIFICATION OF REPORT	18. SECURITY CLASSIFICATION OF THIS PAGE	19. SECURITY CLASSIFICATION OF ABSTRACT	20. LIMITATION OF ABSTRACT
UNCLASSIFIED	UNCLASSIFIED	UNCLASSIFIED	

SUMMARY

In this final report covering the period 1993-1994, the preliminary results of the research on direct numerical simulation of compressible turbulent flows are presented. Specifically, the adaptive Legendre polynomial spectral element method with the mixed explicit-implicit(MEI) Taylor-Galerkin formulation is used in order to capture detailed physics involved in three-dimensional shock wave turbulent boundary layer interactions.

The main activity for the second year was concerned with construction of three-dimensional data structure of the computer program. The material covered in this final report consists of (1) variations of fluctuation velocity components, Reynolds stress contours, and turbulent kinetic energy variations, corresponding to the two-dimensional shock wave turbulent boundary layer interactions examined in the first year progress report and (2) the preliminary results of the three-dimensional flow including the vorticity distributions. Studies on three-dimensional turbulent statistics such as power spectral densities vs wave numbers (or frequencies), spectral energy transfer and cascade, the effects of production and dissipation, inertial subrange, etc. are currently in progress and will be included in the next progress report.

In conclusion, the proposed direct numerical simulation of compressible turbulent flows using the adaptive Legendre polynomial spectral element with the MEI Taylor-Galerkin formulation has been shown to be robust, accurate, and efficient. Further research is required, however, to demonstrate its ultimate impact on CFD through exhaustive examples and comparisons with available experimental data in the future.

TABLE OF CONTENTS

I. INTRODUCTION

The last decade has seen unprecedented technological innovations in computational fluid dynamics, prompted particularly by the increase in technical requirements of aerospace research. Namely, the flowfields due to high velocities, compressibility, shock waves, turbulence, and high temperature have been the focus of intensive research in the past [1-9].

When shock waves interact with turbulent boundary layers in external or internal flows special considerations are required due to widely disparate time and length scales, corresponding to different physical phenomena - namely, turbulence microscales and shock wave surface discontinuities. Here we are faced with the smallest time and length scales which may severely affect the computational requirements. To cope with such requirements various numerical strategies have been developed using finite difference methods (FDM) and finite element methods (FEM). Incorporated or implemented into either FDM or FEM are the finite volume methods (FVM) and spectral element methods (SEM). Modeling of turbulence has been the controversial subject. Closure models, probability density functions (PDF), large eddy simulation (LES), direct numerical simulation (DNS), and other methods have been reported.

The purpose of the present study is to demonstrate the superiority of DNS combined with unstructured adaptive spectral element methods in dealing with combined turbulence and shock waves for both internal and external flows of aerospace vehicles.

This work is motivated by the fact that DNS can be achieved via adaptive h-p methods, combining the mesh refinement (h-method) with spectral polynomial degrees of freedom (p-method). It is well known that the most crucial aspect of turbulent flows is microscales involved in boundary layers (viscous sublayer, buffer zone, and turbulent core). This is where the spectral polynomial degrees of freedom can be increased as desired since the mesh refinement alone is incapable of resolving the microscale requirements. In this way, turbulence modeling techniques can be avoided. Furthermore, the current practice in DNS to use extensive refinements in finite difference discretization may also be avoided. Babuska and his co-workers [10-12] and Oden and his co-workers [13-15] contributed to the advancement of FEM h-p adaptive methods. Their applications have not been extended to shock waves interacting with turbulent boundary layers.

Chung, et al. [16-19] have studied finite element strategies as applied to shock wave turbulent boundary layer interactions in reacting flows and explored applications of direct numerical simulation in characterizing the shock wave turbulent boundary layer interaction. The main emphasis in the present study is to establish the basic theory and computational strategies involved in the Legendre polynomial spectral element method and to present preliminary computational results. Development of theory and formulations include irregular node connectivity of Legendre polynomials of various orders. Comparisons with experimental results have demonstrated superiority of the direct numerical simu-

lation over the standard K-ϵ model with compressibility effects.

In what follows we discuss the governing equations and solutions of Navier-Stokes system of equations via mixed explicit-implicit (MEI) Taylor-Galerkin methods in Section 2, direct numerical simulation with h-p adaptive methods in Section 3, calculations of DNS perturbation variables in Section 4, calculations of flowfield-dependent implicitness parameters and stability analysis in Section 5, numerical applications in Section 6, and conclusions in Section 7.

II. GOVERNING EQUATIONS AND SOLUTIONS OF NAVIER-STOKES SYSTEM OF EQUATIONS

A convenient form of governing equations for compressible viscous flows may be written in terms of conservation variables as follows:

$$\frac{\partial \boldsymbol{U}}{\partial t} + \frac{\partial \boldsymbol{F}_i}{\partial x_i} + \frac{\partial \boldsymbol{G}_i}{\partial x_i} = \boldsymbol{B} \tag{1}$$

where

$$\boldsymbol{U} = \begin{bmatrix} \rho \\ \rho v_j \\ \rho E \end{bmatrix} \qquad \boldsymbol{F}_i = \begin{bmatrix} \rho v_i \\ \rho v_i v_j + p\delta_{ij} \\ \rho E v_i + p v_i \end{bmatrix} \qquad \boldsymbol{G}_j = \begin{bmatrix} 0 \\ -\tau_{ij} \\ -\tau_{ij} v_j + q_i \end{bmatrix} \qquad \boldsymbol{B} = \begin{bmatrix} 0 \\ \rho F_j \\ \rho F_j v_j \end{bmatrix}$$

with standard definitions given by

$$\tau_{ij} = \mu \left(v_{i,j} + v_{j,i} - \frac{2}{3} v_{k,k} \delta_{ij} \right)$$

$$E = e + \frac{1}{2} v_j v_j \,, \qquad e = c_p T - p/\rho \,, \qquad q_i = -k T_{,i}$$

$$\mu = \mu_\infty \frac{T_\infty + S_0}{T + S_0} \left(\frac{T}{T_\infty} \right)^{3/2} \,, \qquad S_0 = 110\, K \,, \qquad k = \frac{c_p \mu}{Pr}$$

$$p = \rho R T$$

The solution of governing equations will be carried out using the Taylor-Galerkin approach with test and trial functions given by isoparametric and Legendre polynomials by means of mixed explicit/implicit schemes. In general, explicit schemes are inexpensive but less accurate in comparison with implicit schemes for regions of high pressure or velocity gradients. In case of rapid variations of gradients throughout the domain it is often desirable to devise a scheme in which implicitness can be adjustable in accordance with gradients, more implicit for the region of high gradients and less implicit or fully explicit for the region of low gradients.

In expanding U^{n+1} in Taylor series about U^n, we introduce the implicitness parameters s_1 and s_2 for the first and second derivatives of U with respect to time [17-19], respectively,

$$U^{n+1} = U^n + \Delta t \frac{\partial U^{n+s_1}}{\partial t} + \frac{\Delta t^2}{2} \frac{\partial^2 U^{n+s_2}}{\partial t^2} + O(\Delta t^3)$$

with

$$\frac{\partial U^{n+s_1}}{\partial t} = \frac{\partial U^n}{\partial t} + s_1 \frac{\partial \Delta U^{n+1}}{\partial t}, \quad 0 \le s_1 \le 1 \tag{3a}$$

$$\frac{\partial^2 U^{n+s_2}}{\partial t^2} = \frac{\partial^2 U^n}{\partial t^2} + s_2 \frac{\partial^2 \Delta U^{n+1}}{\partial t^2}, \quad 0 \le s_2 \le 1 \tag{3b}$$

Substituting (3) into (2) yields

$$\Delta U^{n+1} = \Delta t \left(\frac{\partial U^n}{\partial t} + s_1 \frac{\partial \Delta U^{n+1}}{\partial t} \right) + \frac{\Delta t^2}{2} \left(\frac{\partial^2 U^n}{\partial t^2} + s_2 \frac{\partial^2 \Delta U^{n+1}}{\partial t^2} \right) + O(\Delta t^3) \tag{4}$$

It follows from (1) that

$$\frac{\partial U}{\partial t} = -\frac{\partial F_i}{\partial x_i} - \frac{\partial G_i}{\partial x_i} + B \qquad (5)$$

Here F_i is a function of U and G_i is a function of U and its gradient $U_{,k}$, so that we denote the convective Jacobian a_i, dissipative Jacobian b_i, and dissipative gradient Jacobian c_{ik} as

$$a_i = \frac{\partial F_i}{\partial U} , \quad b_i = \frac{\partial G_i}{\partial U} , \quad c_{ik} = \frac{\partial G_i}{\partial V_k} = \frac{\partial G_i}{\partial U_{,k}}$$

The second derivative of U with respect to time may now be written in terms of these Jacobians.

$$\frac{\partial^2 U}{\partial t^2} = a_i \frac{\partial}{\partial x_i}\left(\frac{\partial F_j}{\partial x_j} + \frac{\partial G_j}{\partial x_j} - B\right) + b_i \frac{\partial}{\partial x_i}\left(\frac{\partial F_j}{\partial x_j} + \frac{\partial G_j}{\partial x_j} - B\right) + c_{ik} \frac{\partial^2}{\partial x_i \partial x_k}\left(\frac{\partial F_j}{\partial x_j} + \frac{\partial G_j}{\partial x_j} - B\right) \qquad (6)$$

Substituting (5) and (6) into (4) yields

$$\Delta U^{n+1} = \Delta t\left[-\frac{\partial F_i^n}{\partial x_i} - \frac{\partial G_i^n}{\partial x_i} + B^n + s_1\left(-\frac{\partial \Delta F_i^{n+1}}{\partial x_i} - \frac{\partial \Delta G_i^{n+1}}{\partial x_i} + \Delta B^{n+1}\right)\right]$$

$$+ \frac{\Delta t^2}{2}\left\{\left[(a_i + b_i)\frac{\partial}{\partial x_i}\left(\frac{\partial F_j^n}{\partial x_j} + \frac{\partial G_j^n}{\partial x_j} - B^n\right) + \frac{\partial B^n}{\partial t}\right] + s_2\left[(a_i + b_i)\frac{\partial}{\partial x_i}\left(\frac{\partial \Delta F_j^{n+1}}{\partial x_j} + \frac{\partial \Delta G_j^{n+1}}{\partial x_j} - \Delta B^{n+1}\right)\right]\right\} + O(\Delta t^3) \qquad (7)$$

In order to provide different implicitness (different amount of damping or dissipation) to different physical quantities, we reassign s_1 and s_2 associated with G_i, respectively

$$s_1 \Delta G_i \rightarrow s_3 \Delta G_i , \qquad s_2 \Delta G_i \rightarrow s_4 \Delta G_i \qquad (8a,b)$$

with the various implicitness parameters defined as

$$\begin{aligned} s_1 &= \textit{first order convective implicitness parameter} \\ s_2 &= \textit{second order convective implicitness parameter} \\ s_3 &= \textit{first order dissipative implicitness parameter} \\ s_4 &= \textit{second order dissipative implicitness parameter} \end{aligned} \qquad (8c)$$

These implicitness parameters play a significant role with

s_1 and s_2 controlling shock discontinuity resolutions and s_3 and s_4 dictating turbulent eddy microscale resolutions. The implicitness parameters are considered to be dependent not only on time but also on space. In particular, s_1 and s_2 are associated with Mach number changes, whereas s_3 and s_4 depend on Reynolds number changes between time steps and between upstream and downstream locations. Further details of these implicitness parameters are given in Section 5.

Neglecting the third order spatial derivatives of conservation variables associated with $\mathbf{c}_{ik}$ in (7) and substituting (8a, b) into (7) lead to the residual,

$$\boldsymbol{R} = \Delta \boldsymbol{U}^{n+1} + s_1 \Delta t \left(\boldsymbol{a}_i \frac{\partial \Delta \boldsymbol{U}^{n+1}}{\partial x_i} - \Delta \boldsymbol{B}^{n+1} \right) + s_3 \Delta t \left(\boldsymbol{b}_i \frac{\partial \Delta \boldsymbol{U}^{n+1}}{\partial x_i} + \boldsymbol{c}_{ij} \frac{\partial^2 \Delta \boldsymbol{U}^{n+1}}{\partial x_i \partial x_j} \right)$$

$$- s_2 \frac{\Delta t^2}{2} (\boldsymbol{a}_i \boldsymbol{a}_j + \boldsymbol{b}_i \boldsymbol{a}_j) \frac{\partial^2 \Delta \boldsymbol{U}^{n+1}}{\partial x_i \partial x_j} - s_4 \frac{\Delta t^2}{2} \left[(\boldsymbol{a}_i \boldsymbol{b}_j + \boldsymbol{b}_i \boldsymbol{b}_j) \frac{\partial^2 \Delta \boldsymbol{U}^{n+1}}{\partial x_i \partial x_j} \right] + \Delta t \left(\frac{\partial \boldsymbol{F}_i^n}{\partial x_i} + \frac{\partial \boldsymbol{G}_i^n}{\partial x_i} - \boldsymbol{B}^n \right)$$

$$- \frac{\Delta t^2}{2} \left\{ (\boldsymbol{a}_i + \boldsymbol{b}_i) \left[\frac{\partial}{\partial x_i} \left(\frac{\partial \boldsymbol{F}_j^n}{\partial x_j} + \frac{\partial \boldsymbol{G}_j^n}{\partial x_j} - \boldsymbol{B}^n \right) \right] + \frac{\partial \boldsymbol{B}^n}{\partial t} \right\} + 0(\Delta t^3) = 0 \qquad (9)$$

where all Jacobians $\mathbf{a}_i$, $\mathbf{b}_i$ and $\mathbf{c}_{ij}$ are assumed to remain constant spatially within each time step and to be updated at subsequent time steps.

The Galerkin integral of (9) may now be carried out as follows:

$$\int_{\Omega} \Phi_\alpha \boldsymbol{R}(\boldsymbol{U}, \boldsymbol{F}_i, \boldsymbol{G}_i) \, d\Omega = 0 \qquad (10)$$

where Φ_α refers to the spectral test functions, and the conservation variables are interpolated by the spectral trial functions Φ_α given by the combination of isoparametric functions and Legendre polynomials as

$$U(x,t) = \Phi_\alpha(x)\,U_\alpha(t), \quad F_i(x,t) = \Phi_\alpha(x)\,F_{\alpha i}(t), \quad G_i(x,t) = \Phi_\alpha(x)\,G_{\alpha i}(t) \tag{11}$$

Substituting (11) into (9) and (10) yields

$$(A_{\alpha\beta}\delta_{rs} + B_{\alpha\beta rs})\Delta U^{n+1}_{\beta s} = H^n_{\alpha r} + N^{n+1}_{\alpha r} + \hat{N}^n_{\alpha r} \tag{12}$$

$$A_{\alpha\beta} = \int_\Omega \Phi_\alpha \Phi_\beta \, d\Omega$$

$$B_{\alpha\beta rs} = \int_\Omega \left\{ \Delta t \left[-s_1 a_{irs} \Phi_{\alpha,i}\Phi_\beta - s_3 \left(b_{irs}\Phi_{\alpha,i}\Phi_\beta + c_{ijrs}\Phi_{\alpha,i}\Phi_{\beta,j} \right) \right] + \frac{\Delta t^2}{2} \left[s_2 \left(a_{irq}a_{jsq} + b_{irq}a_{jsq} \right) + s_4 \left(a_{irq}b_{jsq} + b_{irq}b_{jsq} \right) \right] \Phi_{\alpha,i}\Phi_{\beta,j} \right\} d\Omega$$

$$H^n_{\alpha r} = \int_\Omega \left\{ \Delta t \left[\Phi_{\alpha,i}\Phi_\beta \left(F^n_{\beta ir} + G^n_{\beta ir} \right) + \Phi_\alpha \Phi_\beta B^n_{\beta r} \right] - \frac{\Delta t^2}{2} \left(a_{irs} + b_{irs} \right) \left[\Phi_{\alpha,i}\Phi_{\beta,j} \left(F^n_{\beta js} + G^n_{\beta js} \right) - \Phi_\alpha \Phi_{\beta,i} B^n_{\beta s} \right] - \frac{\Delta t}{2} \Phi_\alpha \Phi_\beta \Delta B^n_{\beta s} \right\} d\Omega$$

$$N^{n+1}_{\alpha r} = \int_\Gamma \left\{ \Delta t \left[-s_1 a_{irs} \overset{*}{\Phi}_\alpha \Delta U^{n+1}_s n_i - s_3 \left(b_{irs} \overset{*}{\Phi}_\alpha \Delta U^{n+1}_s n_i + c_{ijrs} \overset{*}{\Phi}_\alpha \Delta U^{n+1}_{s,j} n_i \right) \right] + \frac{\Delta t^2}{2} \left[s_2 \left(a_{irq}a_{jsq} + b_{irq}a_{jsq} \right) \overset{*}{\Phi}_\alpha \Delta U^{n+1}_{s,j} n_i + s_4 \left(a_{irq}b_{jsq} + b_{irq}b_{jsq} \right) \overset{*}{\Phi}_\alpha \Delta U^{n+1}_{s,j} n_i \right] \right\} d\Gamma$$

$$\hat{N}^n_{\alpha r} = -\int_\Gamma \left[\Delta t \overset{*}{\Phi}_\alpha \left(F^n_{ir} + G^n_{ir} \right) n_i - \frac{\Delta t^2}{2} \left(a_{irs} + b_{irs} \right) \overset{*}{\Phi}_\alpha \left(F^n_{js,j} + G^n_{js,j} \right) n_i \right] d\Gamma$$

Here N^{n+1} terms on RHS of (12) are assembled into boundary nodes of $B_{\alpha\beta rs}$ on LHS. Notice also that indices i, j, k = 1, 2

associated with the Jacobians imply directional identification of each Jacobian matrix (a_1, a_2, b_1, b_2, c_{11}, c_{12}, c_{21}, c_{22}) with r,s = 1, 2, 3, 4 denoting entries of each of the 4x4 Jacobian matrices. It should be warned, however, that these Jacobian matrices must be multiplied precisely as dictated by summing through repeated indices, not through matrix multiplications as a whole.

It is interesting to note that all implicitness parameters can be shown to be functions of flowfields between upstream and downstream, and that the convection implicitness parameters s_1 and s_2 associated with the first term in $B_{\alpha\beta rs}$ are analogous to the total variation diminishing (TVD) limiter in the FDM literature (see Appendix A). With an adequate choice of these implicitness parameters, acceptable resolutions of shock waves have been verified.

On the other hand, the diffusion implicitness parameters s_3 and s_4 are capable of alleviating and accommodating the stiffness involved in turbulent diffusion or finite rate chemistry (if reacting). No analogy can be shown since they do not exist in other numerical schemes. It should also be noted that interactions between convection and diffusion are achieved by means of the terms associated with the products $a_{irq}\, b_{jsq}$ and $b_{irq}\, a_{jsq}$. These terms are particularly important for shock wave turbulent boundary layer interactions where the effect of convection upon diffusion and vice versa is crucial in order to resolve turbulence microscales as disturbed by shock wave interactions. We shall refer to these terms as convection-

diffusion interaction terms.

For low Mach number flows density variations become insignificant. In this case the flow is essentially incompressible and checkerboard type pressure oscillations occur unless a suitable computational scheme is devised to ensure the mass conservation. In the present study the implicitness parameters as calculated from the flowfield are expected to accommodate the conservation of mass and prevent pressure oscillations. In this vein, the effect of compressibility will also be automatically accommodated for high Mach number flows.

III. DNS VIA UNSTRUCTURED h-p ADAPTIVE METHODS

Our objective here is to resolve time and length scales involved in turbulence interacting with shock waves using the unstructured h-p adaptive spectral element methods. One approach is to refine the mesh (h-methods) until further refinement is unproductive, at which time the spectral degrees of freedom (p-methods) are increased in order to reduce errors as desired, such as in the region of turbulent viscous sublayer. However, the more desirable approach is to optimize between the mesh refinement and spectral orders. Thus, the most crucial aspect of the h-p methods is to determine the best possible change in the mesh structure to reduce the local error to a minimum. Should h (mesh size) be decreased or should p (polynomial or spectral degrees of freedom) be increased? Although some work in optimization between the h- and p- processes has been reported

[13-15], the subject of optimization appears to be an open question. Thus, our approach in this study is to refine the mesh until shock waves are adequately computed and then resort to the p- version with higher order Legendre polynomials in order to resolve turbulence microscales. Toward this end, the error indicator e may be defined in terms of density for shock waves and velocity for turbulence. Some of the options are given as follows:

$$\theta = h \max_{\Omega_e} |\rho|_{H^2} / |\rho|_{H^1} \tag{13a}$$

$$\theta = h \max_{\Omega_e} |v_i|_{H^2} / |v_i|_{H^1} \tag{13b}$$

where h is the mesh parameter and various Sobolev space (H^m) seminorms are defined as

$$|\rho|_{H^1} = \left(\int_{\Omega_e} \frac{\partial \rho}{\partial x_i} \frac{\partial \rho}{\partial x_i} d\Omega \right)^{\frac{1}{2}}, \quad |\rho|_{H^2} = \left(\int_{\Omega_e} \frac{\partial^2 \rho}{\partial x_i \partial x_j} \frac{\partial^2 \rho}{\partial x_i \partial x_j} d\Omega \right)^{\frac{1}{2}} \tag{14a}$$

$$|v_i|_{H^1} = \left(\int_{\Omega_e} \frac{\partial v_i}{\partial x_j} \frac{\partial v_i}{\partial x_j} d\Omega \right)^{\frac{1}{2}}, \quad |v_i|_{H^2} = \left(\int_{\Omega_e} \frac{\partial^2 v_i}{\partial x_j \partial x_k} \frac{\partial^2 v_i}{\partial x_j \partial x_k} d\Omega \right)^{\frac{1}{2}} \tag{14b}$$

The choice among these options depends on various physical aspects of the given problem, whether local errors are dominated by density, velocity components, their gradients, or second derivatives. For the purpose of the examples dealt with in Section 5, we utilize Eq. (13a) and Eq. (13b) for the h-adaptivity associated with shock waves and the p- adaptivity associated with turbulent boundary layers, respectively.

Direct numerical simulations for turbulent flows are achieved by higher spectral orders using Legendre polynomials

[10-12]. The spectral element interpolation functions for the corner nodes, side modes, and interior modes in a two-dimensional 4-node isoparametric element are as follows (see Fig. 1a):

Four corner node functions:

$$\Phi_1^{(c)} = \frac{1}{4}(1-\xi)(1-\eta) \quad , \quad \Phi_2^{(c)} = \frac{1}{4}(1+\xi)(1-\eta)$$
$$\Phi_3^{(c)} = \frac{1}{4}(1+\xi)(1+\eta) \quad , \quad \Phi_4^{(c)} = \frac{1}{4}(1-\xi)(1+\eta) \tag{15}$$

Side mode functions:

$$N^{(SM)} = 4(p-1), \quad i=2,\ldots p$$
$$\Phi_m^{(s1)} = \frac{1}{2}(1-\eta)G_m(\xi) \quad , \quad \Phi_m^{(s2)} = \frac{1}{2}(1+\xi)G_m(\eta)$$
$$\Phi_m^{(s3)} = \frac{1}{2}(1+\eta)G_m(\xi) \quad , \quad \Phi_m^{(s4)} = \frac{1}{2}(1-\xi)G_m(\eta) \tag{16}$$

Interior mode functions (bubble functions):

$$N^{(I)} = \frac{(p-2)(p-3)}{2}, \quad p \geq 4$$
$$\Phi_{mn}^{(I)} = G_m(\xi)G_n(\eta) \quad , \quad m,n = 2,\ldots p, \quad m+n \leq p \tag{17}$$

where $N^{(SM)}$ and $N^{(I)}$ denote, respectively, the total number of interpolation functions available for sides n (1,2,3,4) and the interior, p is the highest Legendre polynomial order chosen, and the Legendre interpolation functions, $G_m(\xi)$ and $G_m(\eta)$, are defined in terms of the Legendre polynomials $\rho_i(\xi)$ as follows:

$$G_m(\xi) = \frac{1}{\sqrt{2(2m-1)}}(\rho_m(\xi) - \rho_{m-2}(\xi)) \tag{18}$$

The same procedure applies to the η-direction.

Notice that the corner node interpolation functions are

linear whereas the side modes and interior modes depend on the order p of Legendre polynomials chosen. For a three-dimensional domain tensor products in the third direction ζ for a hexahedral element can be constructed similarly as in the two-dimensional case, but with surface mode functions as well as edge and interior mode functions.

As a consequence of these Legendre polynomials representing the side and interior mode functions, any variable U may be modeled as

$$U = \Phi_\alpha U_\alpha + \Phi_m^{(SM)} \hat{U}_m + \Phi_{mn}^{(I)} \hat{U}_{mn} \tag{19}$$

where $\Phi_m^{(SM)}$ and $\Phi_{mn}^{(I)}$ denote the side and interior mode functions, respectively, and $\hat{U}_m$ and $\hat{U}_{mn}$ are spectral coefficients to be calculated from additional integrals,

$$\int_\Omega \Phi_m^{(SM)} R(U)\, d\Omega = 0 \tag{20a}$$

$$\int_\Omega \Phi_{mn}^{(I)} R(U)\, d\Omega = 0 \tag{20b}$$

Here the standard static condensation may be used to eliminate $\hat{U}_m$ and $\hat{U}_{mn}$. Thus the final form of the finite element equations is modified to

$$(A_{\alpha\beta}\delta_{r\beta rs} + B_{r\beta rs})\,\Delta U_{\beta s}^n = H_{\alpha r}^n - W_{\alpha r}^n + N_{\alpha r}^{n+1} + \hat{N}_{\alpha r}^n \tag{21}$$

where $W_{\alpha r}^n$ acts as a source term reflecting the Legendre polynomial side and interior mode functions obtained from the static condensation of (12), (20a), and (20b). In this way,

variables are calculated only at the corner nodes, regardless of high order Legendre polynomial approximations.

Our objective here is to satisfactorily simulate turbulent microscales within an element. All side mode and interior mode interpolation functions vanish at the corner nodes but exhibit high frequency variations according to the order of Legendre polynomials along the sides and interior domain. It is intended that such Legendre polynomial microscales be capable of simulating the physical microscales of turbulence such as those of Kolmogorov and Taylor (Fig. 1b). Microscales involved in viscous sublayer, buffer zone, and turbulent core are of the order of 10^{-1} mm whereas characteristic lengths of domain of interest may be over meters or kilometers. Thus the h-adaptivity alone is severely limited and naturally we seek a remedy of this situation in the h-p adaptivity utilizing the highest spectral orders required for accuracy.

Transition elements involve irregular nodes in the h-refinement process -- node c for element T-1 and nodes c and d for element T-2 as shown in Fig. 1c. To assure linear approximations for both unrefined and refined elements, we must eliminate irregular nodes involved in the unrefined elements. This can be done simply by assuming [13]

$$U_c = \frac{1}{2}(U_Q + U_R), \qquad U_d = \frac{1}{2}(U_R + U_S) \tag{22}$$

This will lead to

$$U^{(T-1)} = \Phi_N^{(c)} H_{NM}^{(T-1)} U_M^{(T-1)} \quad (N,M = 1,2,3,4) \tag{23a}$$

$$U^{(T-2)} = \Phi_N^{(c)} H_{NM}^{(T-2)} U_M^{(T-2)} \qquad (N,M = 1,2,3,4) \tag{23b}$$

where $H_{NM}^{(T-1)}$ and $H_{NM}^{(T-2)}$ denote the auxiliary matrices for T-1 and T-2 elements, respectively,

$$H_{NM}^{(T-1)} = \begin{bmatrix} \frac{1}{2} & 0 & 0 & \frac{1}{2} \\ 0 & 1 & 0 & 0 \\ 0 & 0 & 1 & 0 \\ 0 & 0 & 0 & 1 \end{bmatrix} \qquad H_{NM}^{(T-2)} = \begin{bmatrix} 1 & 0 & 0 & 0 \\ \frac{1}{2} & \frac{1}{2} & 0 & 0 \\ 0 & 0 & 1 & 0 \\ \frac{1}{2} & 0 & 0 & \frac{1}{2} \end{bmatrix} \tag{24}$$

and $U_M^{(T-1)}$ and $U_M^{(T-2)}$ are the unknown nodal vectors in terms of the global nodes Q, R, and S with the irregular nodes c and d eliminated.

The advantage of Legendre polynomials is an ease in dealing with side and interior modes which do not require specification of nodes physically located. This is especially beneficial for side modes in establishing boundary continuities. Continuity of variables and gradients along the inter-element boundaries is to be dictated by the higher order polynomials between the two adjacent elements.

Similar extensions can be made for three-dimentional geometries. The three-dimensional Legendre polynomial spectral element configuration is shown in Fig. 1d. It is seen that side modes and the interior mode of a 2-D element become edge modes and face modes for a 3-D element, respectively. These modes are in addition to the 3-D interior mode.

IV. DNS PERTURBATION VARIABLES

It is well known that DNS is expected to provide information in turbulence microscale levels at the expense of excessive

refinements of domain discretization [6]. The purpose of the present study is, instead, to avoid such refinements by means of implementing high spectral Legendre polynomial orders. The Navier-Stokes solver as introduced here allows unsteady time accurate solutions from which perturbation variables (f') can be calculated as the difference between the Navier-Stokes solution (f) and its time average $\bar{f}$ [20, 21],

$$f' = f - \bar{f} \tag{25}$$

This computation can be conducted throughout the Navier-Stokes integration time steps or upon arrival at quasi-steady state. Strictly speaking, in shock wave/turbulent boundary layer interactions a complete steady state is never realized as unsteady eddy motions persist indefinitely, although background flowfields may become steady. This is referred to as the quasi-steady state. The time average of Navier-Stokes solution is performed using the Gaussian quadrature. In this process complicated physical phenomena such as homogeneous and inhomogeneous, isotropic and anisotropic, and nonstationary nature of perturbation flowfields for a compression corner with shock wave turbulent boundary layer interactions can be resolved.

Furthermore, all perturbation variables as calculated from (25) can be transformed via fast Fourier transform to generate power spectral density vs frequency domain. In section 6 we examine various perturbation variables as well as background flowfield data. As a result of this study, more details of shock wave turbulent boundary layer interactions such as variations of

turbulent kinetic energy vs shock strength, laminar-turbulence transition instability, relaminarization, effects of dilatation, etc., can be rigorously examined in comparison with the previous investigations [6, 22-23]. Some limited results and discussion of these subjects are presented in Section 5.

V. CALCULATIONS OF FLOWFIELD-DEPENDENT IMPLICITNESS PARAMETERS AND STABILITY ANALYSIS

The success of hp version spectral element method described above depends on accurate calculations of flowfield-dependent implicitness parameters. With appropriate choices of nodal points in a one-dimensional case it was demonstrated in Section 2 that the terms associated with the convection-implicitness parameters (s_1, s_2) in the MEI formulation are analogous to the the FDM-TVD methods. To further examine both convection and diffusion implicitness parameters we propose the following criteria:

$$s_1, s_2 = \begin{cases} \min(r,1) & r > \alpha \\ 0 & r < \alpha \\ 1 & M_{\min} = 0 \end{cases} \tag{25}$$

with

$$r = \frac{\Delta M}{M_{\min}} \tag{26}$$

where ΔM is the difference between the maximum and minimum Mach number ($\Delta M = M_{max} - M_{min}$) within a finite element, and α is a user-specified small number ($\alpha \sim 0.01$).

$$s_3, s_4 = \begin{cases} \min(s,1) & s > \beta \\ 0 & s < \beta \\ 1 & Re_{(min)} = 0 \end{cases} \tag{27}$$

with

$$s = \frac{\Delta Re}{Re_{(min)}}, \quad \beta = 0.01 \tag{28}$$

where ΔRe is the difference between the maximum and minimum Reynolds number ($\Delta Re_{(max)} - \Delta Re_{(min)}$) within a finite element and ß is a user-specified small number (ß ≈ 0.01). For reacting flows, the diffusion parameters s_3 and s_4 are also calculated from Damköhler numbers using the similar criteria as in (27) and (28). Depending upon the length and time scales involved in the actual flowfield, the diffusion implicitness parameters are governed by either turbulence or finite rate chemistry, whichever are larger if chemical reactions are included.

As a result of both convection and diffusion implicitness parameters based on the flowfield variables, it is possible to derive an expression for the amplification factor for (12) in one dimension in the form

$$G = \frac{1 + \left[(1-s_3)C^2 + 2(1-s_3)\frac{C}{Re} - 3(1-s_4)\right]\frac{C^2}{Re^2}(\cos\phi - 1) + I(s_1 - 1)C\sin\phi}{1 + \left[-s_2C^2 - \frac{2s_3C}{Re} + \frac{3s_4C^2}{Re^2}\right](\cos\phi - 1) + Is_1C\sin\phi} \tag{29}$$

with

$$C = \frac{a\Delta t}{h}, \quad Re = \frac{ah}{\nu}, \quad \phi \equiv k_m h = \frac{\pi m h}{L}, \quad I = \sqrt{-1}$$

For illustration, the amplification factors for various modes m versus courant number C are shown in Fig. 2. It is

evident that stability conditions are much more favorable than those given in [32] where only the convection implicitness parameters were considered. It is also shown that as the Reynolds number decreases stability increases for intermediate modes (m=0.5) with an increase of diffusion implicitness parameters s3 and s4.

VI. APPLICATIONS

In the 1993 progress report, the validity of the use of Legendre polynomial spectral elements in conjunction with adaptive mesh refinements was demonstrated using two example problems (flat plate and compression corner). Fourth order Legendre polynomials were used for direct numerical simulation of these problems. In that report the results of turbulent statistics were not presented.

In Fig.3, the perturbution velocity components corresponding to the flate plate shock wave turbulent boundary interactions, page 37, the 1993 progress report are shown. These variables are in a random unsteady state within the boundary layer (solid line) and more or less steady state outside the boundary layer (dashed line). Here, one unit of nondimensional time is equivalent to 0.96 ms, and thus the unsteady motion frequencies vary from approximately 62 to 135 kHz for the streamwise component and 31 to 94 kHz for the spanwise component.

Fig.4 shows perturbation normal and shear stress components, indicating that shock wave turbulent boundary layer interactions contribute to dilation (compressibility effect) as evidenced by greater normal stresses than sheal stresses.

Also of interest, as shown in Fig.5, is the sharp rise of turbulent kinetic energy in the boundary layer, away from the wall but slightly below the boundary layer, where shock-turbulence interactions are maximum, indicating the amplification of turbulent kinetic energy.

The major achievement of the past year is the completion of computer algorithm for the three-dimensional data structure. To check out this algorithm a three-dimensional sharp-leading-edged fin has been investigated for swept shock wave turbulent boundary layer interactions. Fig.6a shows the physical domain for a 3-D sharp fin (α=20) and a general flowfield structure (Fig.6b,c) [33]. The inlet boundary conditions are the same as used by Knight et al. [34] and the corresponding flowfield structure. Here the free stream Mach number and temperature are M_∞=2.93 and T_∞=92.39 K, corresponding to the chamber pressure and temperature of 680 kPa and 251 K, respectively, with the Reynolds number being 7×10^8 /m. The boundary layer thickness δ_o at the apex of the fin is 1.4cm, yielding a Reynolds number $Re_{\delta o}$= 9.8×10^5. In order to match the boundary conditions as used for the experiments [34] the flowfied behind the fin is calculated as a flat plate boundary layer such that the computed boundary layer thickness δ_o is set equal to the experimental value of 1.4 cm. On the solid surfaces no slip and adiabatic wall boundary conditions are applied. On the upper, lateral, and at downstream exit boundaries the flow variables are set free. Adaptively spaced grid points are 33, 41, and 31 in the streamwise, spanwise, and vertical directions, respectively. No attempt is made for further adaptive refinements for the geometry shown in Fig.6d at this time.

Fig.7 shows the background flowfield based on the geometric configurations and boundary conditions described in Fig.6, as observed from the front (x-z and y-z faces). As such, no details of the hidden portion are shown. Subject to the detailed examination in comparison with the experimental data to be given in Fig.8, we are only able to detect a general qualitative trend of the flowfield in Fig.7. It is to be noticed that the trend is in reasonable agreement with the results of Narayanswami et al. [35], with density and pressure increasing drastically along the shock waves, the temperature rise being distributed along the flat plate, and Mach number sharply decreasing through the shock waves toward the flat-plate boundary.

Fig.8 shows comparisons of yaw angles at various locations : (a) x=7.549 cm, y=-6.1087cm and (b) x=8.827cm, y=-7.3787cm with the experimental and other computational data [34]. As pointed out in [34] uncertainties in the experimental data (portion of broken line) obscure the comparison not only with the other computational data (turbulence models) but also with the pressent study. Further investigation is required, however, to determine the cause of these deviations.

Vorticity variations at different planes are shown in Figs. 9 through 11. The contours of vorticity component in the streamwise planes (y-z planes) in the x-direction with each plane identified as a,b,c,d,e are shown in Fig.9. The corresponding velocity vectors are plotted on the right-hand-side. Clearly, the vortex stretching occurs toward downstream with the evidence of separation shocks, slip lines, and vortex centers close to the wall. These physical phenomena become more significant toward downstream in agreement with the skematics shown in Figs.6b and c.

Fig.10 shows the contours of vorticity component in the spanwise vertical planes (x-z planes) in the y-direction, with each plane idendified as a,b,c,d. The vortex stretching occurs again toward downstream and moving upward along the shock. The growth of vorticity is concentrated within the boundary layer close to the wall.

In Fig.11 the spanwise horizontal plane vorticity contours are presented at various locations (a : $2\delta_o$, b : δ_o, c : $0.5\delta_o$) where δ_o is the boundary layer thickness. It is seen that vorticity increases toward the wall with its intensity increasing toward downstream as expected.

VII. CONCLUSIONS

Based on the preliminary results obtained for the direct numerical simulation using the MEI Taylor-Galerkin Legendre polynomial spectral element method, it appears that our original goal for the initial attempt has been successfully achieved. The main concern was to make certain that the irregular node connectivity of the h-p process can numerically be implemented. Elaborate data structure schemes which have been developed are the

major factor for these achievements. In addition, the preliminary results for three-dimensional computations of sharp fin shock wave turbulent boundary layer interactions are satisfactory.

There are still many more tasks remaining unexplored. They include: (1) verification of 3-D fluctuations, unsteadiness, and turbulent micro-scales as related to turbulent Mach number, turbulent Prandtl number, and turbulent Reynolds number, (2) characterization of compressibility effects and relaminarization, (3) energy spectrum data versus frequency domain and complete 3-D turbulent statistics, (4) laminar-turbulence transition instability, (5) reliable optimal control of h-p interactions with Legendre polynomials, (6) temporal and spatial dependency of implicitness parameters, among others. They constitute challenging future tasks in years to come. In summary, it is concluded that the direct numerical simulation for turbulent compressible flows with the Legendre polynomial spectral element method appears to be promising.

Appendix A

ANALOGY BETWEEN MEI SCHEME AND FDM-TVD

For simplicity, consider a one-dimensional Euler equation

$$\frac{\partial u}{\partial t} + a\frac{\partial u}{\partial x} = 0 \qquad \text{(A1)}$$

The MEI equation for (A1) with derivatives written in terms of nodes u_i, u_{i-1}, and u_{i-2} becomes

$$\frac{\Delta u_i^{n+1}}{\Delta t} = -\frac{s_1 a}{\Delta x}\left(\Delta u_i^{n+1} - \Delta u_{i-1}^{n+1}\right) + \frac{s_2 aC\Delta x}{2\Delta x^2}\left(\Delta u_i^{n+1} - 2\Delta u_{i-1}^{n+1} + \Delta u_{i-2}^{n+1}\right)$$

$$- \frac{1}{\Delta x}\left(f_i^n - f_{i-1}^n\right) + \frac{C\Delta x}{2\Delta x^2}\left(f_i^n - 2f_{i-1}^n + f_{i-2}^n\right) \qquad \text{(A2)}$$

where C is the Courant number, $C = a\Delta t/\Delta x$.

The FDM-TVD equation for (A1) may be written as

$$\frac{du_i}{dt} = -\frac{a^+}{\Delta x}\left[(u_i - u_{i-1}) + \frac{1}{2}\Psi^-_{i-\frac{1}{2}}(u_i - u_{i-1}) - \frac{1}{2}\Psi^-_{i-\frac{3}{2}}(u_{i-1} - u_{i-2})\right]$$

$$- \frac{a^-}{\Delta x}\left[(u_{i+1} - u_i) + \frac{1}{2}\Psi^-_{i+\frac{1}{2}}(u_{i+1} - u_i) - \frac{1}{2}\Psi^-_{i+\frac{3}{2}}(u_{i+2} - u_{i-1})\right] \qquad \text{(A3)}$$

with

$a^+ = \max(0,a) = 1/2\ (a + |a|)$

$a^- = \min(0,a) = 1/2\ (a - |a|)$

Introducing an implicitness parameter s for the time derivative on RHS of (A3) in the form

$$u_i = u_i^n + s\Delta u_i^{n+1} \qquad \text{(A4)}$$

Substituting (A4) into (A3) and assuming that

$$a^- = 0, a^+ = a, \Psi^+_{i-\frac{1}{2}} = \Psi^+_{i-\frac{3}{2}} = \Psi$$

for simplicity, we obtain

$$\frac{\Delta u_i^{n+1}}{\Delta t} = -\frac{sa}{2\Delta x}(\Delta u_i^{n+1} - \Delta u_{i-1}^{n+1}) - \frac{s\Psi a\Delta x}{2\Delta x^2}(\Delta u_i^{n+1} - 2\Delta u_{i-1}^{n+1} + \Delta u_{i-1}^{n+1})$$

$$- \frac{1}{\Delta x}(f_i^n - f_{i-1}^n) - \frac{\Psi\Delta x}{2\Delta x^2}(f_i^n - 2f_{i-1}^n + f_{i-2}^n) \qquad \text{(A5)}$$

Comparing (A2) and (A4) reveals that

$$s_1 = \frac{s}{2}, \quad s_2 = -\frac{s}{C}\Psi, \quad C = -\Psi, \quad s_2 = s = 2s_1.$$

It is clear that the MEI formulation and FDM-TVD scheme are analogous; in fact, they are identical under the assumptions made above. The implicitness parameters s_1 and s_2 in the MEI scheme play the role of TVD limiters, Ψ. However, the implicitness parameters s_3 and s_4, beyond the concept of TVD scheme, are expected to govern complex physical phenomena such as turbulent boundary layer interactions with shock waves, finite rate chemistry, widely disparate length and time scales, compressibility effects in high Mach number flows, etc. Undoubtedly, all implicitness parameters are flowfield dependent with s_1 and s_2 associated with Mach numbers, s_3 and s_4 with Reynolds numbers and Damkohler numbers, between upstream and downstream nodes within finite elements.

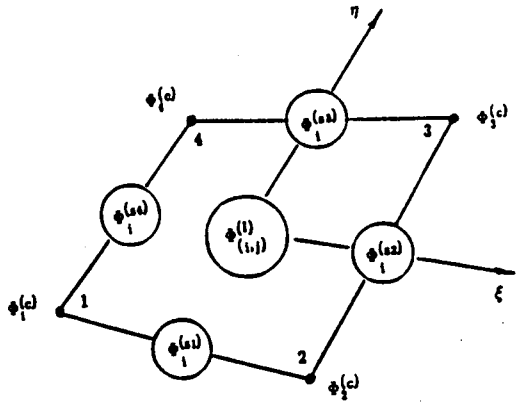

(a) Two-dimensional element

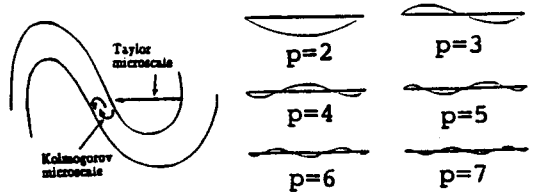

(b) Legendre polynomial microscale

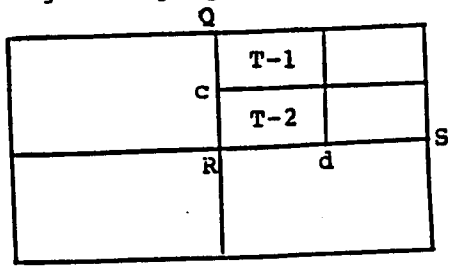

(c) Treatment of irregular nodes

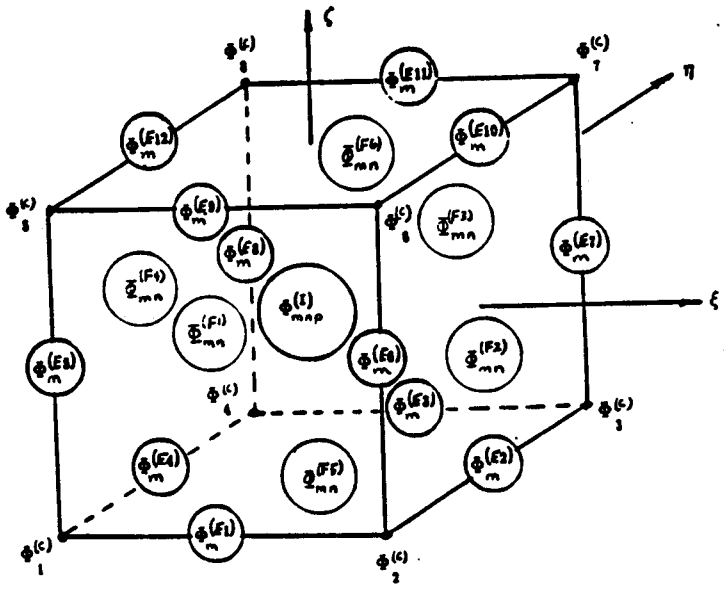

(d) Three-dimensional element

Fig. 1 Spectral element functional representation for Legendre polynomials

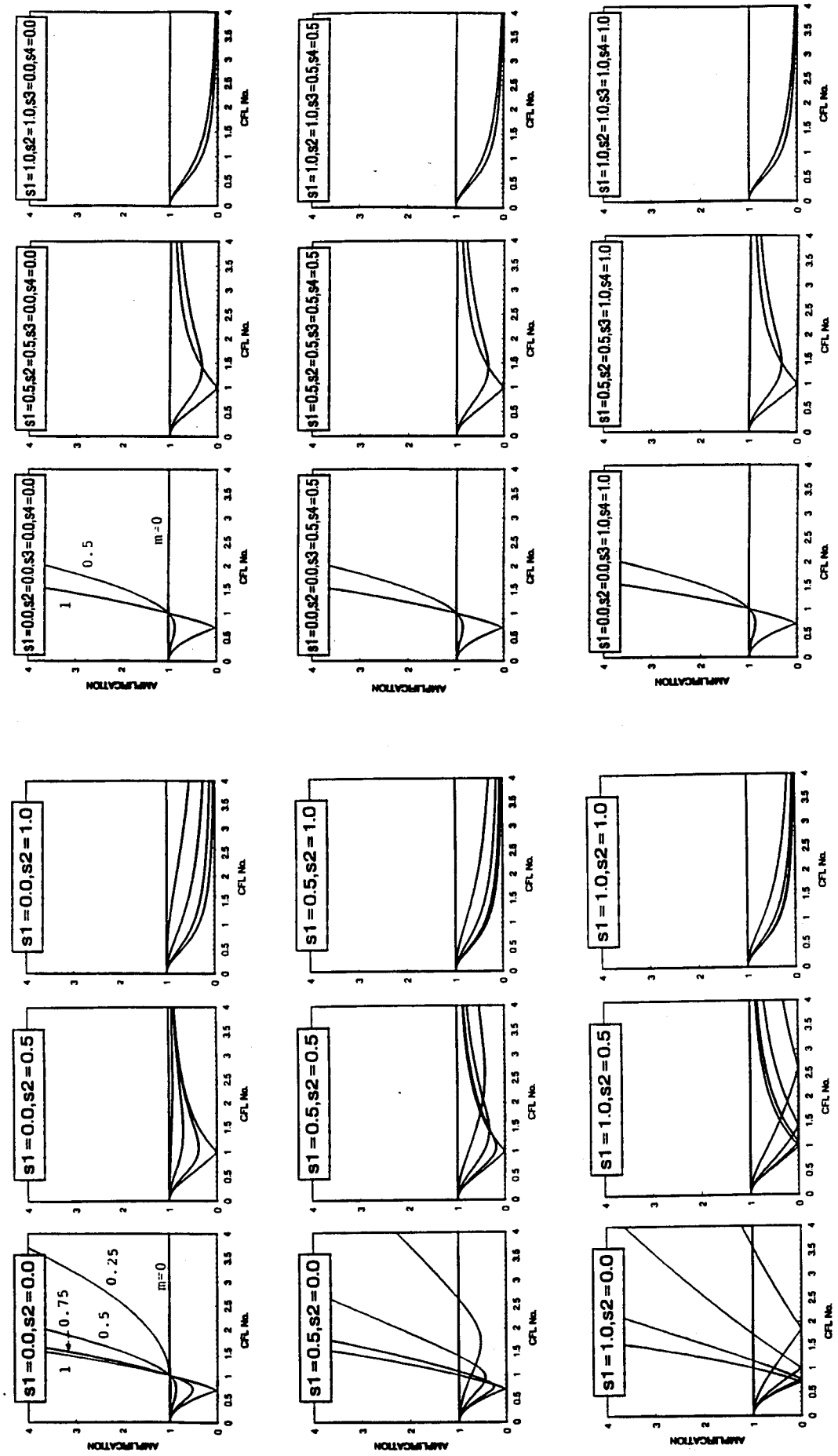

Von Neumann stability analysis of MEI schemes for $Re=\infty$

Von Neumann stability analysis of MEI schemes for $Re=10^4$

Fig. 2 von Neumann Stability Analysis of MEI Schemes

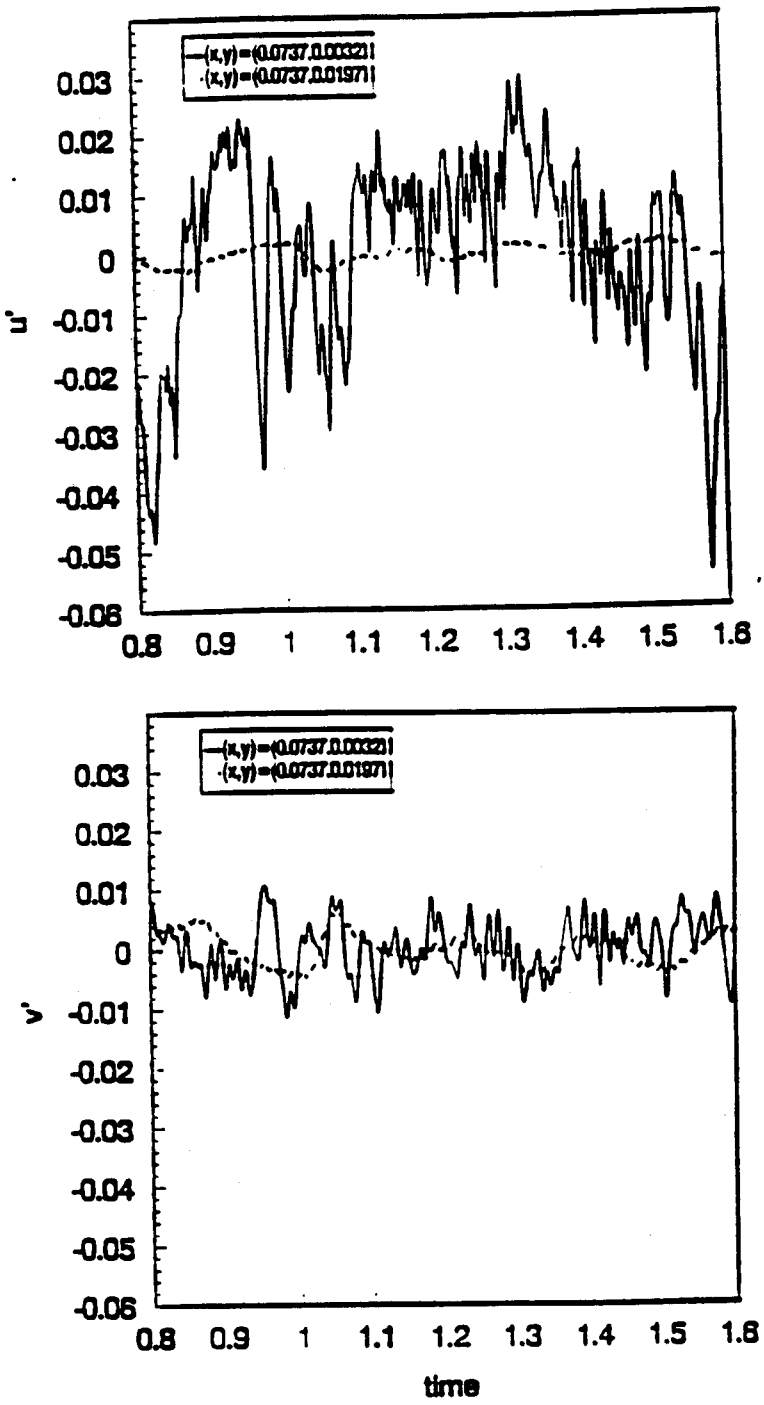

Fig. 3 Perturbation velocity components for the flat plate, page 37, 1993 progress report.

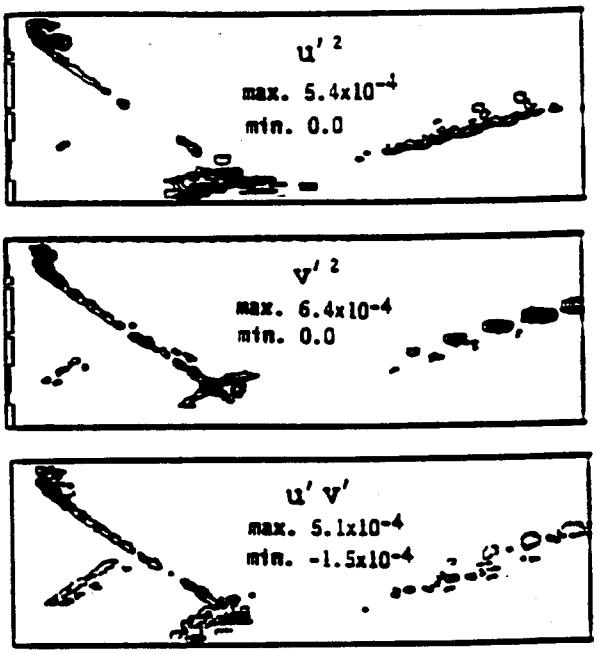

Fig. 4 Reynolds stree components for the flat plate, page 37, 1993 progress report.

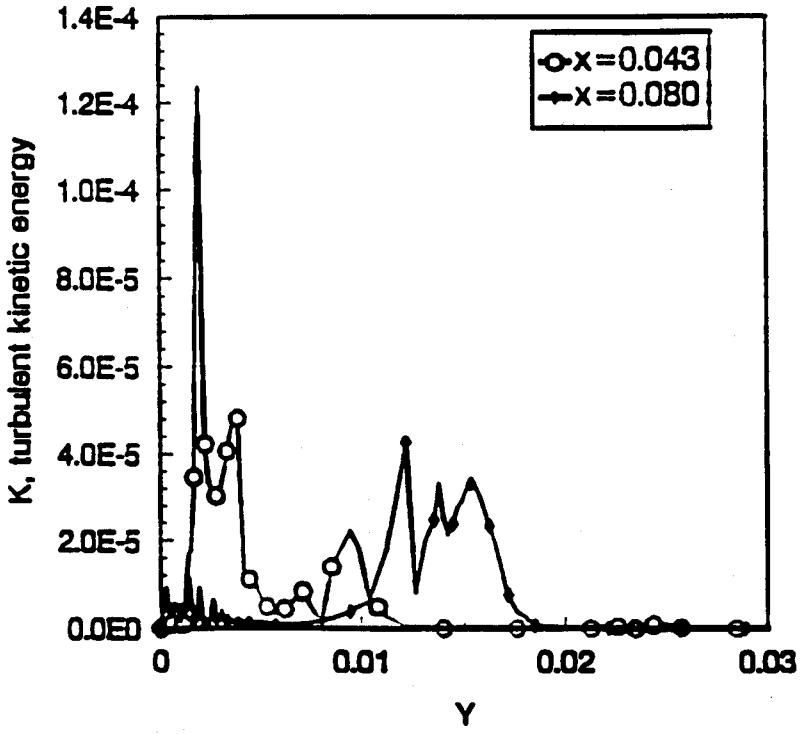

Fig. 5 Turbulent kinetic energy for the flat plate, page 37, 1993 progress report.

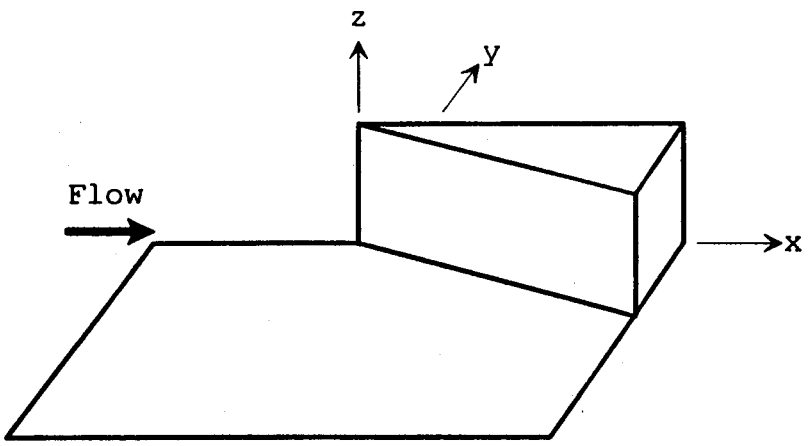

(a) 3-D 20° fin.

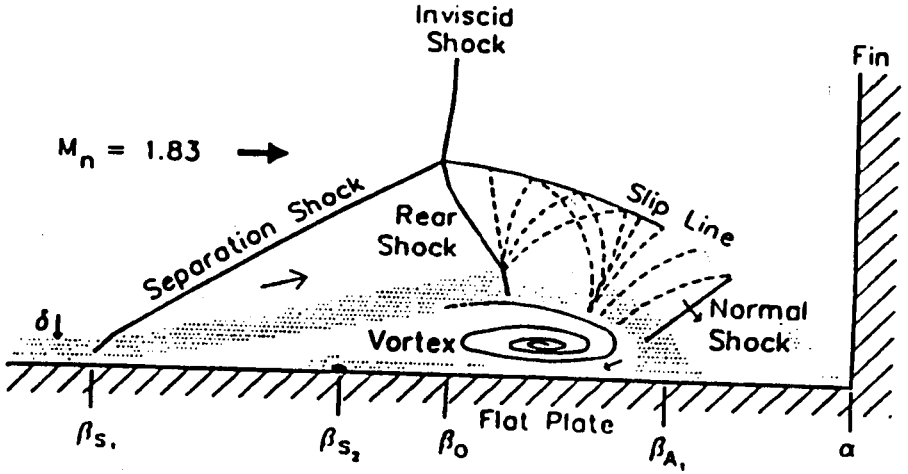

(c) 20° fin interaction flowfield structure.

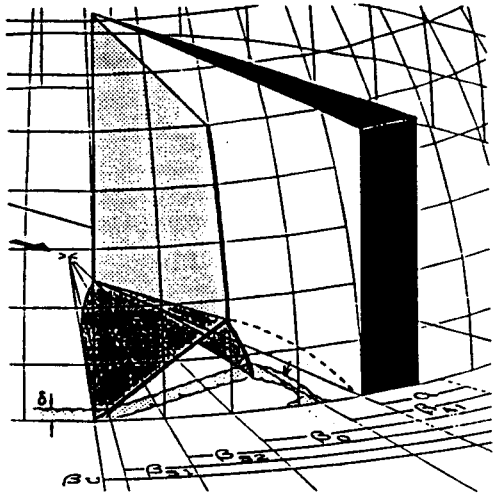

(b) Projection of quasiconical interaction flowfield onto spherical polar coordinate surface.

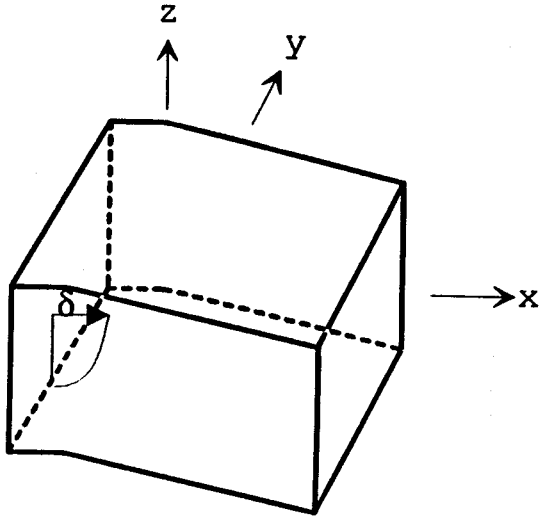

(d) Computational domain for a 3-D 20° fin.

Fig. 6 Computational domain for a 3-D 20° fin and flowfield structure [33], M_∞ = 2.93, P_∞ = 20.57 KPa, T_∞ = 92.39 K, Re = 7 x 10^8 /m.

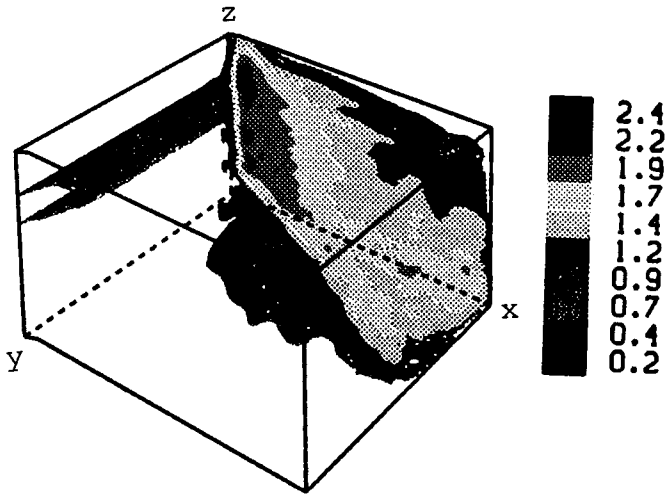

(a) Density (Kg/cm^3).

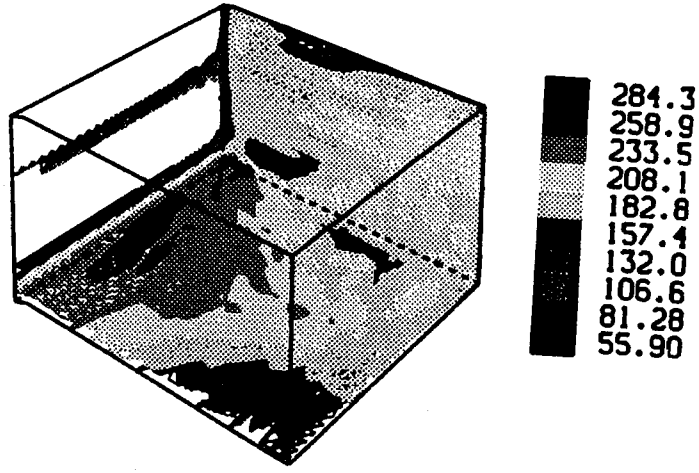

(c) Temperature (K).

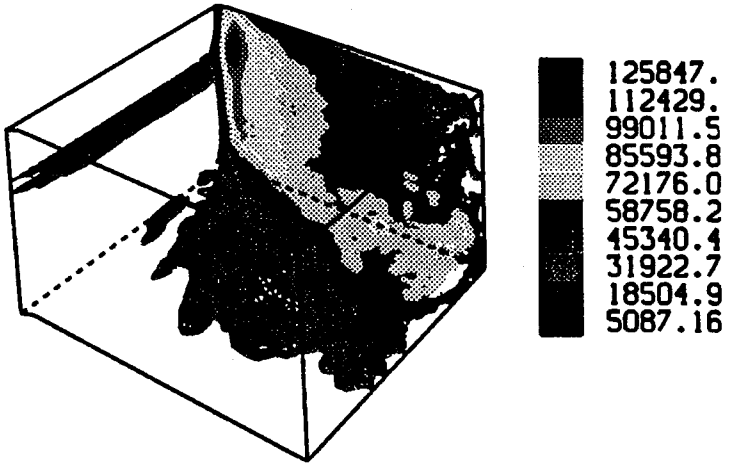

(b) Pressure (Pa).

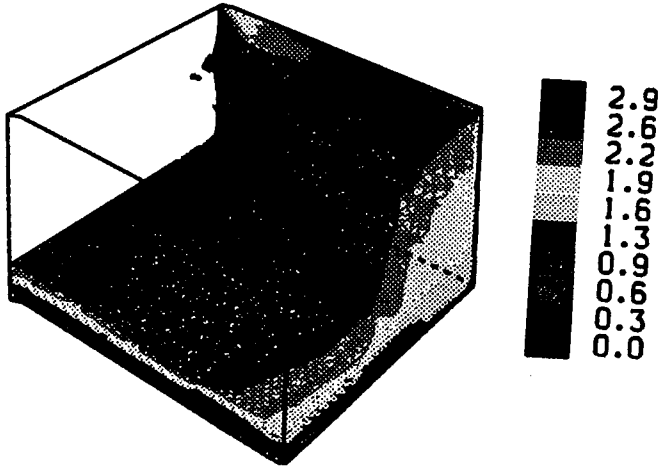

(d) Mach number.

Fig. 7 Background flowfield as observed from the front (x-z plane and y-z plane). (t=0.3965ms)

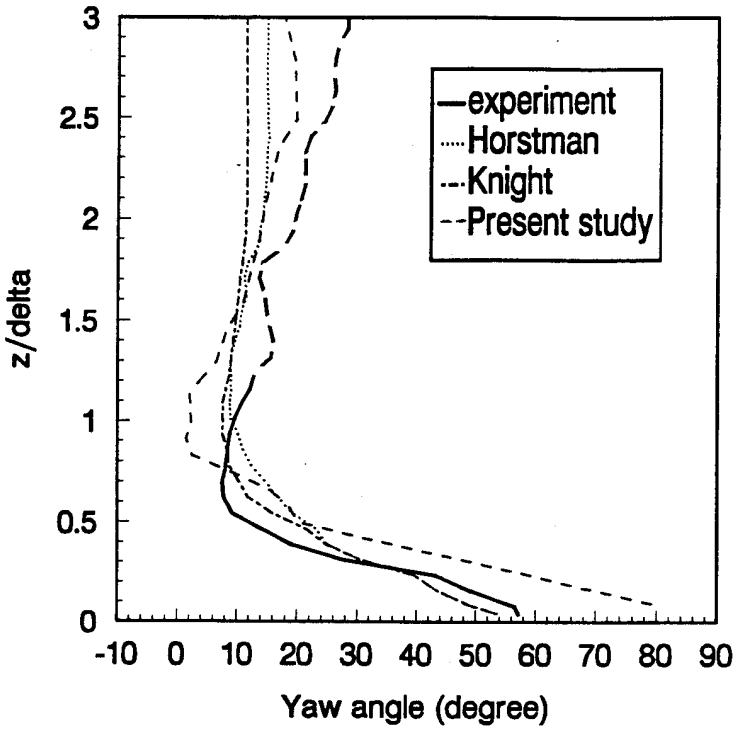

(a) Yaw angle at x=7.549cm and y=-6.1087cm

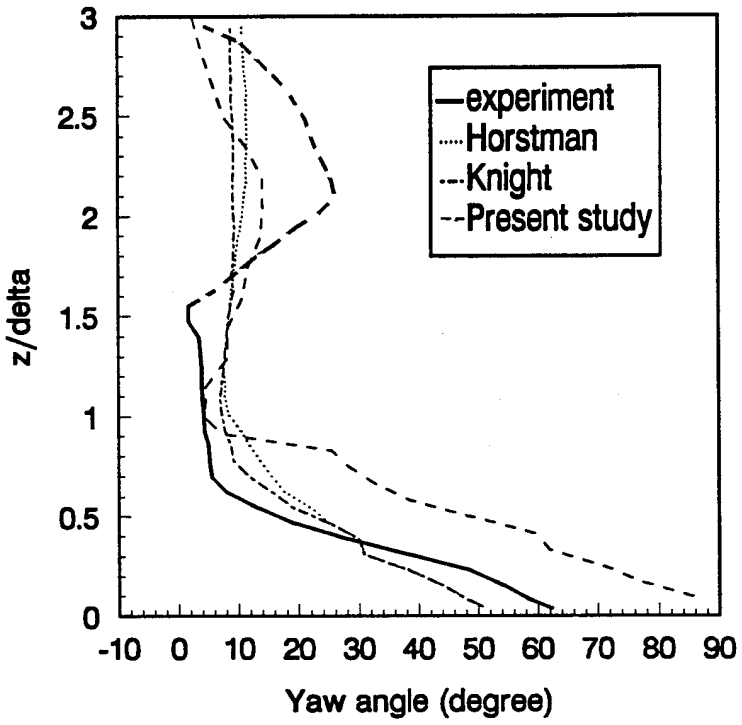

(b) Yaw angle at x=8.827cm and y=-7.3787cm

Fig. 8 Comparisons of yaw angles at various positions

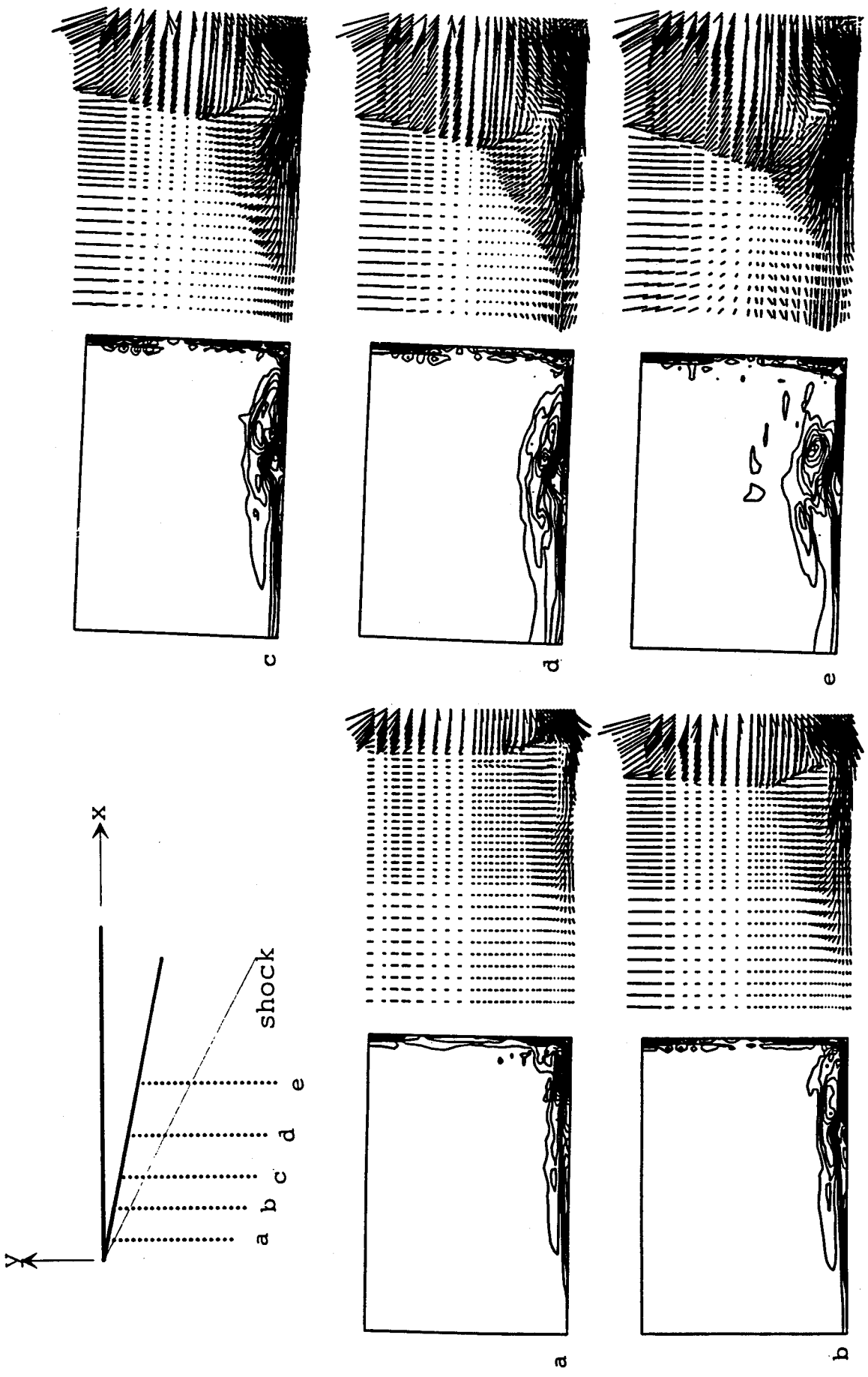

Fig. 9 Streamline vorticity contours and velocity vectors. (t=0.3965ms)

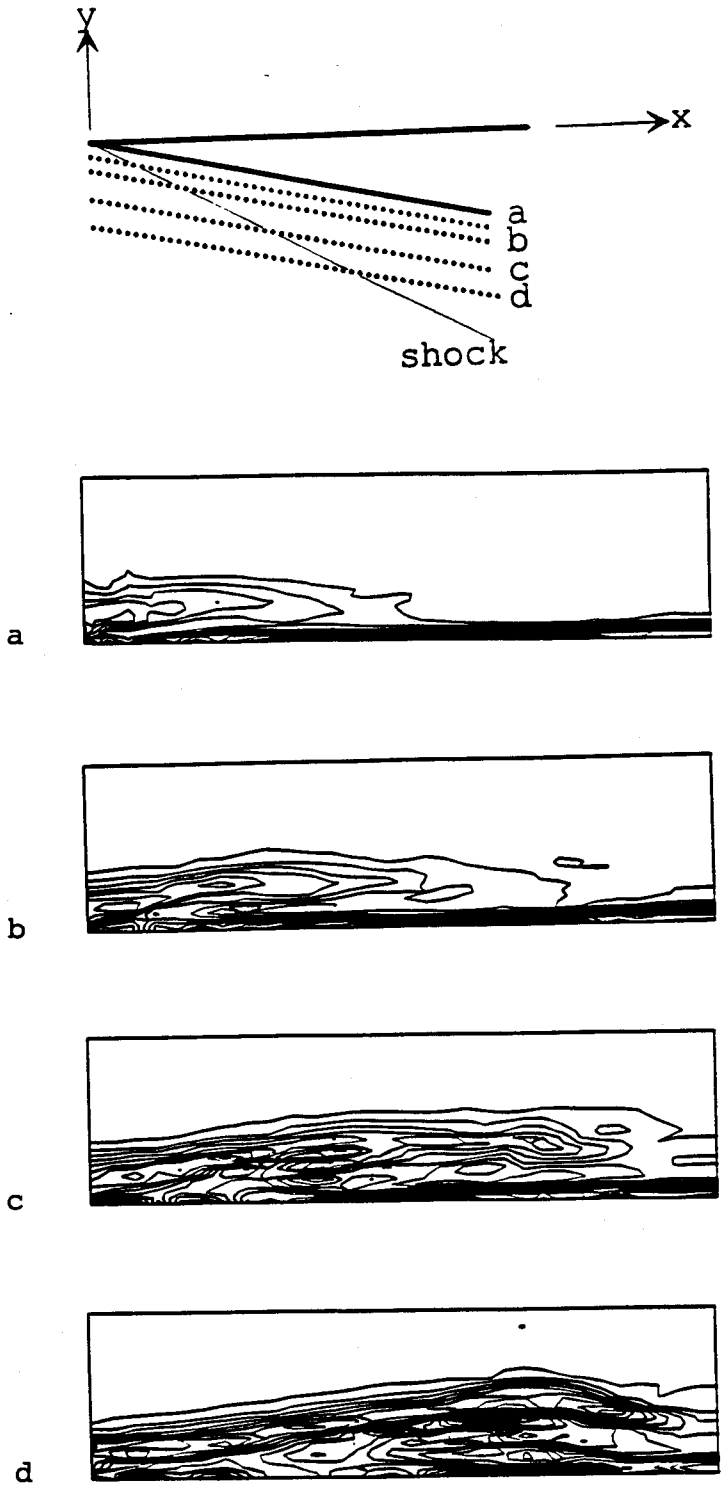

Fig. 10 Spanwise vertical plane (x-z plane) vorticity contours at various locations. (t=0.3965ms, $0 \leq \frac{z}{\delta_o} \leq 2.5$)

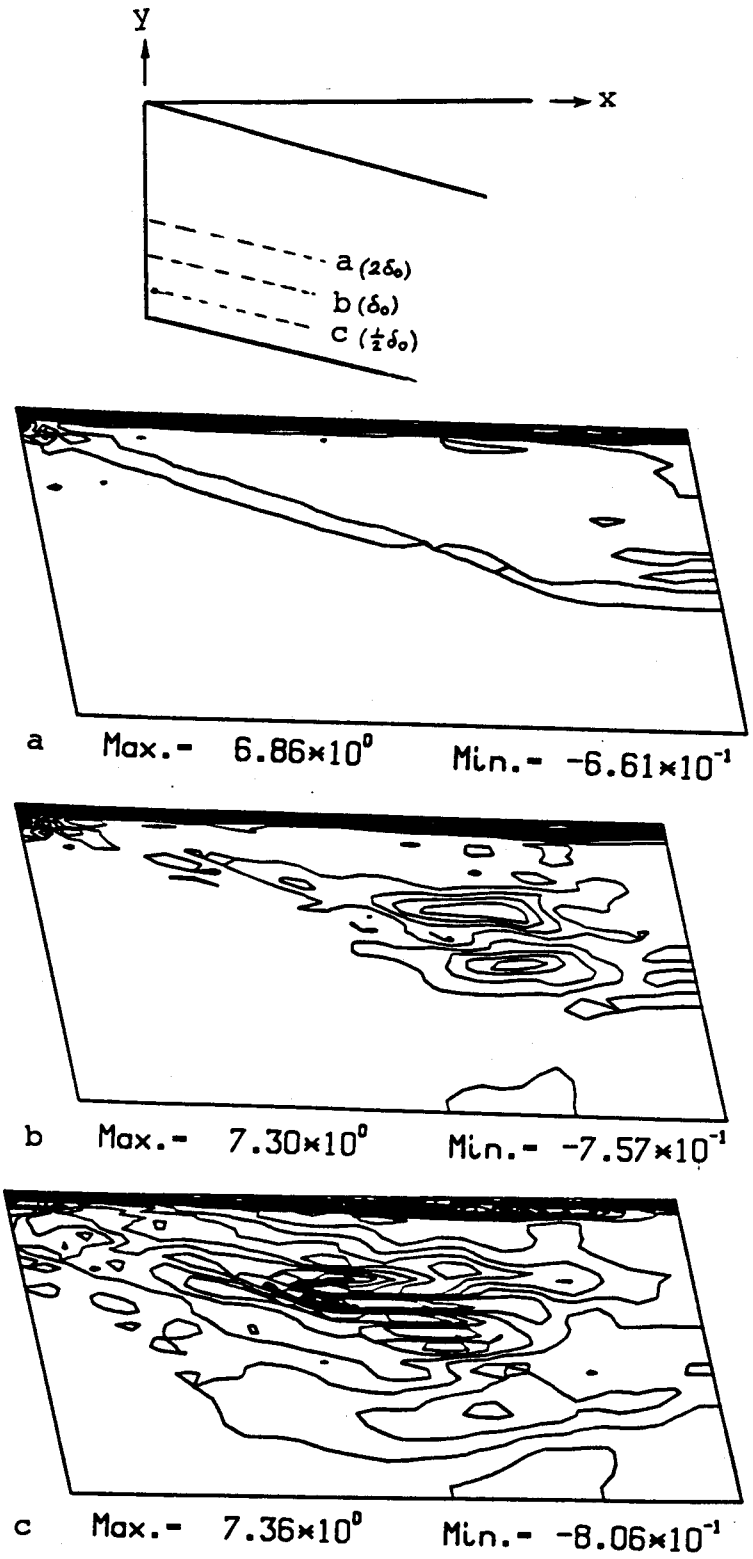

Fig. 11 Spanwise horizontal plane (x-y plane) vorticity contours at various locations. (t=0.3965ms)

REFERENCES

[1]Poddar, K., and Bogdonoff, S., "A Study of Unsteadiness of Crossing Shock ave Turbulent Boundary Layer Interactions," AIAA Paper 90-1456, 1990.

[2]Zeman, O., "Dilatation Dissipation: The Concept and Application of Modeling Compressible Mixing Layers," Physics of Fluids A2(2), February 1990.

[3]Sandham, N.D., and Reynolds, W.C., "Three-dimensional Simulations of Large Eddies in the Compressible Mixing Layer," Journal of Fluid Mechanics, Vol. 224, 1991, pp. 133-158.

[4]Buckingham, A.C., "Interactive Shock Structure Response to Turbulence," AIAA Paper 90-1642, 1990.

[5]Passort, T., and Pouquet, A., "Numerical Simulation of Compressible Homogeneous Flows in the Turbulent Regime," Journal of Fluid Mechanics, Vol. 181, pp. 441-466, 1987.

[6]Lee, S., Lele, S.K., and Moin, P., "Direct Numerical Simulation and Analysis of Shock Turbulence Interaction," AIAA Paper No. 91-0523, 1991.

[7]Sarkar, S., "Application of a Reynolds Stress Turbulence Model to the Compressible Shear Layer," AIAA Paper No. 90-1465, 1990.

[8]Kim, Y.M., and Chung, T.J., "Finite Element Analysis of Turbulent Diffusion Flames," AIAA Journal, Vol. 27, No. 3, 1989, pp. 330-339.

[9]Chung, T.J., and Yoon, W.S., "Effects of Reacting Flows with Turbulence and Shock Waves on Efficiency of Scramjet Combustors,"

28th JANNAF Combustion Meeting, Oct. 18 - Nov. 1, 1991.

[10]Guo, B., and Babuska, I., "The h-p Version of the Finite Element Method, Parts 1 and 2," Comp. Mech, Vol. 1, pp. 21-41, 1986, pp. 203-220.

[11]Babuska, I., and Suri, M., "The h-p Version of the Finite Element Method with Quasi-uniform Meshes," RAIRO Math Mod. and Numerical Analysis 21(2), 1987, pp. 199-238.

[12]Gui, W., and Babuska, I., "The h, p, and h-p Versions of the Finite Element Method in One Dimension, Parts 1, 2, 3," Numerical Mathematics, Vol. 49, 1986, pp. 577-683.

[13]Demkowicz, L., Oden, J.T., Rachowicz, W., and Hardy, O., "Toward A Universal h-p Adaptive Finite Element Strategy, Part 1. Constrained Approximation and Data Structure," Computer Methods in Applied Mechanics and Engineering, Vol. 77, 1989, pp. 79-112.

[14]Oden, J.T., Demkowicz, L., Rachowicz, W., and Westermann, T.A., "Toward a Universal h-p Adaptive Finite Element Strategy, Part 2. A Posteriori Error Estimation," Computer Methods in Applied Mechanics and Engineering, Vol. 77, 1989, pp. 113-180.

[15]Rachowicz, W., Oden, J.T., and Demkowicz, L., "Toward a Universal h-p Adaptive Finite Element Strategy, Part 3. Design of h-p Meshes," Computer Methods in Applied Mechanics and Engineering, Vol. 77, 1989, pp. 181-212.

[16]Chung, T.J., Finite Element Analysis in Fluid Dynamics, McGraw-Hill Book Company, 1978.

[17]Chung, T.J. and Yoon, W.S.," Hypersonic Combustion with Shock Waves in Turbulent Reacting Flows," AIAA paper 92-3426, 1992.

[18]Chung, T.J. and Yoon, W.S., "Numerical Simulations of Airbreathing Combustion at All Speed Regimes," AIAA paper 93-1972.

[19]Chung, T.J. and Yoon, W.S., "Finite Rate Chemical Reactions in Subsonic, Supersonic, and Hypersonic Turbulent Flows," AIAA paper 93-2993.

[20]Chung, T.J. and Yoon, W.S., "Wave Instability in Combustion," Computer Methods in Applied Mechanics and Engineering, Vol. 90, 1991, pp. 583-608.

[21]Yoon, W.S. and Chung, T.J., "Nonlinearly Unstable Waves Dominated by Entropy Mode," Journal of Acoustic Society of America, Vol. 96, No. 2, Pt. 1, August 1994.

[22]Moin, P. and Kim, J., "Numerical Investigation of Turbulent Channel Flow," Journal of Fluid Mechanics, Vol. 118, 1982, pp. 341-377.

[23]Kim, J., Moin, P., and Moser, R., "Turbulence Statistics in Fully Developed Channel Flow at Low Reynolds Number," Journal of Fluid Mechanics, Vol. 177, 1987, pp. 133-166.

[24]Mansour, N.N., Kim, J., and Moin, P., "Reynolds-Stress and Dissipation-Rate Budgets in a Turbulent Channel Flow," Journal of Fluid Mechanics, Vol. 194, 1988, pp. 15-44.

[25]Lele, S.K., "Direct Numerical Simulation of Compressible Free Shear Flows," AIAA-89-0374, 1989.

[26]Zang, T.A., Hussaini, M.Y. and Bushnell, D.M., "Numerical Computations of Turbulence Amplification in Shock Wave Interactions," AIAA Journal, Vol. 22, No. 1, 1984, pp. 13-21.

[27]Lee, M.J., "Distortion of Homogeneous Turbulence by Axisymmetric Strain and Dilatation," Physics of Fluids A, Vol. 1(9), 1989, pp. 1542-1557.

[28]Rotman, D., "Shock Wave Effects on a Turbulent Flow," Physics of Fluids A3, 1991, pp. 1792-1802.

[29]Smits, A.J. and Muck, K.C., "Experimental Study of Three Shock Wave/Turbulent Boundary Layer Interactions," J. Fluid Mechanics, Vol. 182, 1987, pp. 291-314.

[30]Dolling, D.S. and McClure, W.B., "Flowfield Sealing in Sharp Fin-Induced Shock Wave/Turbulent Boundary-Layer Interaction," AIAA Journal, Vol. 23, No. 2, 1985, pp. 201-206.

[31]Dolling, D.S. and Rodi, P.E., "Upstream Influence and Separation Scales in Fin-Induced Shock Turbulent-Layer Interaction," J. Spacecraft, Vol. 25, No. 2, 1988, pp. 102-108.

[32]Tworzydlo, W.W., Oden, J.T., and Thornton, E.A., "Adaptive Implicit/Explicit Finite Element Method for Compressible Viscous Flows," Computer Methods in Applied Mechanics and Engineering, Vol. 95, 1992, pp. 397-440.

[33] Settles, G. S. and Dolling. D.S., "Swept Shock/Boundary Interactions-Tutorial and Update", AIAA Paper 90-0375, 1990.

[34] Knight, D., Horstman, C., and Shapey, B., "The Flowfield Structure of the 3-D Shock Wave-Boundary Layer Interaction Generated by a 20 deg Sharp Finat Mach 3", AIAA 86-0343, 1986.

[35]Narayanswami, N., Horstman, C. C.. and Knight, D. D., "Computation of Crossing Shock/TurbulenceLayer Interaction at Mach 8.3", AIAA Journal,Vol. 31, No. 8, 1993, pp 1369-1376.